ARTICLE

Fast, Simple, Combinatorial Routes to the Fabrication of Reusable, Plasmonically Active Gold Nanostructures by Interferometric Lithography of Self-Assembled Monolayers

Anna Tsargorodska,[†] Osama El Zubir,[†] Brice Darroch,[†] Michaël L. Cartron,[‡] Tamara Basova,[§,∥] C. Neil Hunter,[‡] Alexei V. Nabok,[⊥] and Graham J. Leggett[†,*]

[†]Department of Chemistry, University of Sheffield, Brook Hill, Sheffield S3 7HF, U.K., [‡]Department of Molecular Biology and Biotechnology, University of Sheffield, Western Bank, Sheffield S10 2TN, U.K., [§]Nikolaev Institute of Inorganic Chemistry, SB RAS, 3 Lavrentiev Avenue, Novosibirsk, Russia, [∥]Novosibirsk State University, Pirogova Street 2, Novosibirsk, Russia, and [⊥]Materials and Engineering Research Institute, Sheffield Hallam University, Howard Street, Sheffield S1 1WB, U.K.

ABSTRACT We describe a fast, simple method for the fabrication of reusable, robust gold nanostructures over macroscopic (cm^2) areas. A wide range of nanostructure morphologies is accessible in a combinatorial fashion. Self-assembled monolayers of alkylthiolates on chromium-primed polycrystalline gold films are patterned using a Lloyd's mirror interferometer and etched using mercaptoethylamine in ethanol in a rapid process that does not require access to cleanroom facilities. The use of a Cr adhesion layer facilitates the cleaning of specimens by immersion in piranha solution, enabling their repeated reuse without significant change in their absorbance spectra over two years. A library of 200 different nanostructures was prepared and found to exhibit a range of optical behavior. Annealing yielded structures with a uniformly high degree of crystallinity that exhibited strong plasmon bands. Using a combinatorial approach, correlations were established between the preannealing morphologies (determined by the fabrication conditions) and the postannealing optical properties that enabled specimens to be prepared "to order" with a selected localized surface plasmon resonance. The refractive index sensitivity of gold nanostructures formed in this way was found to correlate closely with measurements reported for structures fabricated by other methods. Strong enhancements were observed in the Raman spectra of tetra-*tert*-butyl-substituted phthalocyanine. The shift in the position of the plasmon band after site-specific attachment of histidine-tagged green fluorescent protein (His-GFP) and bacteriochlorophyll *a* was measured for a range of nanostructured films, enabling the rapid identification of the one that yielded the largest shift. This approach offers a simple route to the production of durable, reusable, macroscopic arrays of gold nanostructures with precisely controllable morphologies.

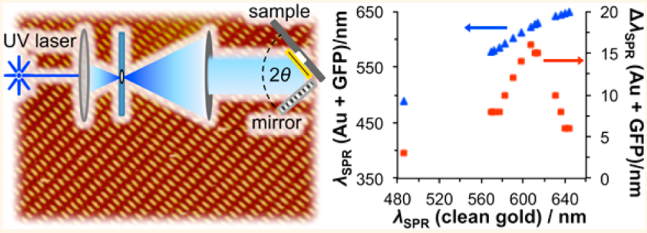

KEYWORDS: nanofabrication · photolithography · plasmonics · self-assembled monolayers · interferometric lithography · gold nanostructures

The field of plasmonics[1,2] has expanded rapidly over the past decade. The optical properties of metal nanostructures are very different from those of bulk materials because of the strong coupling that can occur between oscillations of their surface electrons and incident electromagnetic radiation.[3−9] Nanostructures formed from gold and some other metals may exhibit strong plasmon bands in their optical spectra as a consequence of this coupling, leading to pronounced coloration and dramatic changes in the optical properties of molecules that are placed in close proximity to the metal surface.[8] For example, gold nanoparticles display strong, size- and structure-dependent colors[10] that are subject to modification through nonradiative coupling between neighboring particles.[10−12] These effects have been used in elegant analytical

* Address correspondence to Graham.Leggett@sheffield.ac.uk.

Received for review March 12, 2014 and accepted July 9, 2014.

Published online July 09, 2014
10.1021/nn5014319

systems based on the colorimetric detection of binding between nucleic acids[11,13] and proteins.[14,15] Raman dyes[16,17] and fluorophores may yield greatly enhanced cross sections when coupled to nanostructures.[18−20] Enhancements of 6−8 orders of magnitude have been reported in the Raman scattering cross sections of Raman dyes coupled to gold and silver nanostructures.[21−24]

A number of routes exist for the synthesis of nanoparticles in solution, including the citrate-stabilized reduction of chloroauric acid[25] and the Brust−Schiffrin method.[26] However, for many potential applications of gold nanoparticles in sensing, it is necessary to be able to form well-ordered assemblies of particles on a solid substrate. There are two broad classes of approaches to this. First there are methods that provide great precision, but rely upon rather complex and specialized instrumentation, including electron beam lithography[18] and nanoimprint lithography.[15,27−29] Second, there are approaches that use very simple apparatus, in particular colloidal lithography,[30,31] but where the degree of control over particle spacing, size, and periodicity is more limited. These methods have been used very widely because of their simplicity and low cost.

There has been a great deal of interest in the development of methods that combine precise control over particle morphology and packing, while not requiring the use of costly, specialized apparatus. Photolithography is one approach that has attracted interest.[32,33] Interferometric lithography (IL)[34,35] is an attractive approach because it offers the possibility of carrying out lithographic modification rapidly over macroscopic areas. Moreover, because of the ease with which the exposure parameters may be controlled, it offers a great deal of flexibility and provides, in principle, the possibility for rapid and facile fabrication of a wide range of nanoparticle morphologies. Previously, IL has been used in a conventional lithographic process, to expose photoresist in combination with metal deposition and lift-off.[14,32,36] The use of IL to pattern self-assembled monolayers (SAMs) of alkylthiolates[37] has also been reported, but the fabrication of only one type of structure was reported and no measurements were made of the optical properties.[38]

In the present work we explore the feasibility of using IL to produce a wide range of structures in a combinatorial fashion by direct, double exposure of SAMs and wet etching. The processing methodology relies upon a simple Lloyd's mirror interferometer, consisting of a laser and a small number of simple optical components, and is not carried out under cleanroom conditions. Excellent results are achieved using polycrystalline gold films supported on chromium-primed glass slides, in combination with a mild organic etch (mercaptoethylamine and ammonia in ethanol[39]). The use of a Cr adhesion layer enables multiple reuses of the substrates over periods as long as two years, by cleaning in cold piranha solution. A wide range of structures can be fabricated rapidly in a combinatorial fashion (*ca.* 45−50 min from the as-prepared SAM to the completed nanostructure array). Many of these structures yield strong plasmon bands, and annealing causes recrystallization of the gold so that all specimens yield strong plasmon absorptions. Importantly, the localized surface plasmon wavelength (λ_{SPR}) can be controlled by varying the fabrication conditions. By varying the angle of rotation of the sample between exposures, while maintaining a fixed angle between the interfering beams, or by varying the angle between the interfering beams, it is possible to select the value of λ_{SPR} over a significant range. This enables the selection of the sample with highest sensitivity to a given analyte, demonstrated here for green fluorescent protein and bacteriochlorophyll *a*. Because of the simplicity and speed of the process, we believe it could enable the mass production of inexpensive materials that exhibit strong optical activity over macroscopic areas.

RESULTS AND DISCUSSION

Combinatorial Fabrication of Gold Nanostructures over Macroscopic Areas. SAMs of octadecanethiol (ODT) on gold were photopatterned by interferometric lithography using a Lloyd's mirror two-beam interferometer, as shown in Figure 1. Half of the clean coherent beam was pointed directly onto the sample surface, and the other half of the beam was pointed onto a mirror, from which it was reflected onto the sample surface where it interfered with the other half of the beam to yield a sinusoidal pattern. The period (d) of the resultant interference pattern depends on the wavelength (λ) of the laser used, the (n), and the angle (θ) at which the two beams interfere:[34,35]

$$d = \frac{\lambda}{2 \sin \theta} \quad (1)$$

IL was utilized to fabricate gold nanodots, using double exposures of SAMs on gold. The first exposure was carried out after locating the sample on the stage close to the mirror. SAMs of ODT on 20 nm thick gold films were exposed to between 34 and 54 J cm^{-2} at 244 nm. At the lower limit well-separated samples were formed that did not exhibit plasmon bands in their absorbance spectra; at the upper limit, structures were formed at larger separations. A second exposure was carried out after rotating the sample on the stage through an angle ϕ, as shown in Figure 1b. A dose of 20 J cm^{-2} was used for the second exposure. After photopatterning, the samples were etched using 2-mercaptoethylamine hydrochloride (MEA) (at a concentration of 0.2 mol dm^{-3} and 8% ammonia in ethanol) for 12 min. The total time taken, from the as-prepared SAM to completion of the etching process, was 45−50 min. The angle 2θ between the mirror and sample was set to 60° to yield a period equal to the

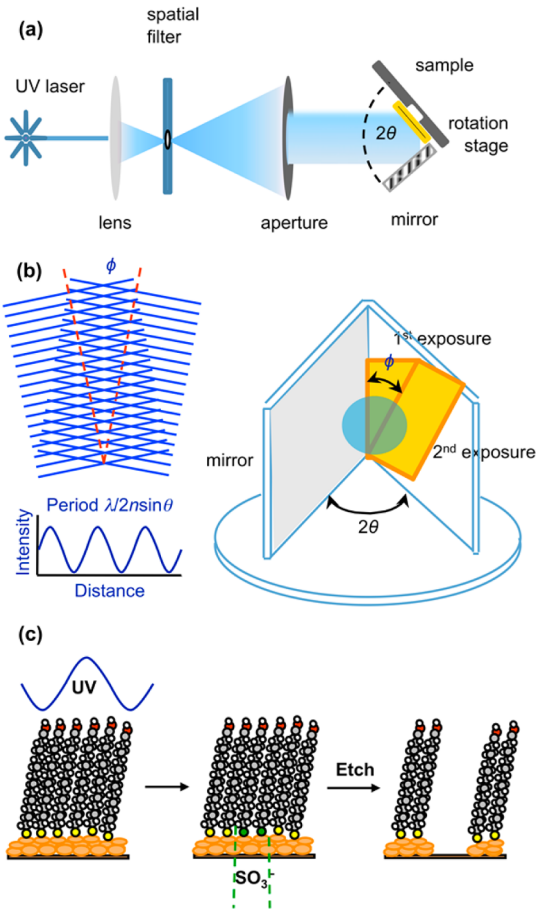

Figure 1. (a) Schematic diagram of a Lloyd's mirror interferometer. (b) Schematic diagrams showing the fabrication of structures using two exposures, with the sample being rotated through an angle ϕ between exposures. (c) Schematic diagram illustrating the use of a SAM as a resist for the etching of nanostructures into a gold film.

laser wavelength for fabrication of relatively large structures to demonstrate the difference in morphology. AFM topographical images of samples formed using different rotations ϕ are shown in Figure 2. For $\phi = 90°$, a square array of dots results, while for $\phi = 60°$, a hexagonal array is formed. As ϕ is decreased further, the structures become elongated until at $\phi = 25°$ parallel rows of needles are formed.

Figure 2g shows an SEM image of a gold nanorod array that was fabricated by two exposures with $\phi = 30°$. This image demonstrates that a high degree of perfection was maintained in the fabrication process over a large area. SEM was used to map samples of 1×1 cm^2 and confirmed the morphology and quality were invariant over areas as large as *ca.* 9×8 mm^2.

A very large variety of structures could be prepared in a combinatorial fashion. A library of 200 different structures was selected for detailed characterization.

Characterization of As-Prepared Nanostructures. Figure 3 shows absorption spectra acquired using a spectrophotometer. In order to achieve good localized surface plasmon absorptions, it is necessary for the separation between nanostructures to be optimal.[40] Samples that were fabricated using $\phi = 90°, 60°$, or $45°$ and exhibited interparticle separations of less than 125 nm (referred to hereafter as type I structures) yielded spectra that were indistinguishable from those recorded for continuous polycrystalline gold films (Figure 3a). In some cases, these samples exhibited small aggregates of residual gold between the nanostructures, as a result of incomplete etching.

As the spacing (the mean distance between nanostructures) increased, LSPR was observed (Figure 3b). Of the samples that exhibited these strong plasmon absorptions (referred to hereafter as type II structures), 95% were fabricated with $\phi = 30°$. Once the parameters (θ, ϕ) that yielded strong plasmon bands had been identified from the library of 200 samples, further samples with identical morphologies and absorbance spectra could be prepared repeatably. Figure 2e and g show, respectively, AFM and SEM images of such structures. The mean aspect ratio (length/breadth) of these structures was 3.4 ± 0.4.

Absorption spectra for these samples had λ_{max} values in the range 480−540 nm. Even where, in some cases, small deposits of gold remained between the structures after etching, strong plasmon bands were observed as a result of the increased separation between the structures. The spectrum in Figure 3b exhibits an absorption maximum at *ca.* 520 and a shoulder at 720 nm, possibly corresponding to the transverse and longitudinal modes, respectively. Detailed analysis suggests that the main peak is in fact composed of two overlapping components. This is possibly explained by the inherent heterogeneity of structures: the nanorods are formed from clusters of gold crystallites, and the absorption band in the experimental spectrum is likely a superposition of the transverse mode of the nanorods and the plasmon absorption of the gold grains from which they are formed. (A high-magnification AFM image is provided in the Supporting Information.) Moreover, the area illuminated by the spectrophotometer is 1 mm^2, and the responses are an average from *ca.* 7×10^6 nanorods. While the resulting integrated signal from such a system reduces the absolute sensitivity compared with individual particles, the system averages are much more consistent than measurements on individual nanorods.

The LSPR wavelength λ_{SPR} of the nanostructures could be varied by changing their size, height, and spacing. Figure 4a shows the variation in λ_{SPR} as a function of the interparticle spacing. In agreement with previously published observations for gold nanostructures prepared by other methods,[40] the resonance wavelength λ_{SPR} increases with spacing, S ($\sim\Delta\lambda/\Delta S \approx 0.16$).

Between these two extremes, intermediate behavior was observed; for these samples, the spectra were different from those of continuous polycrystalline gold

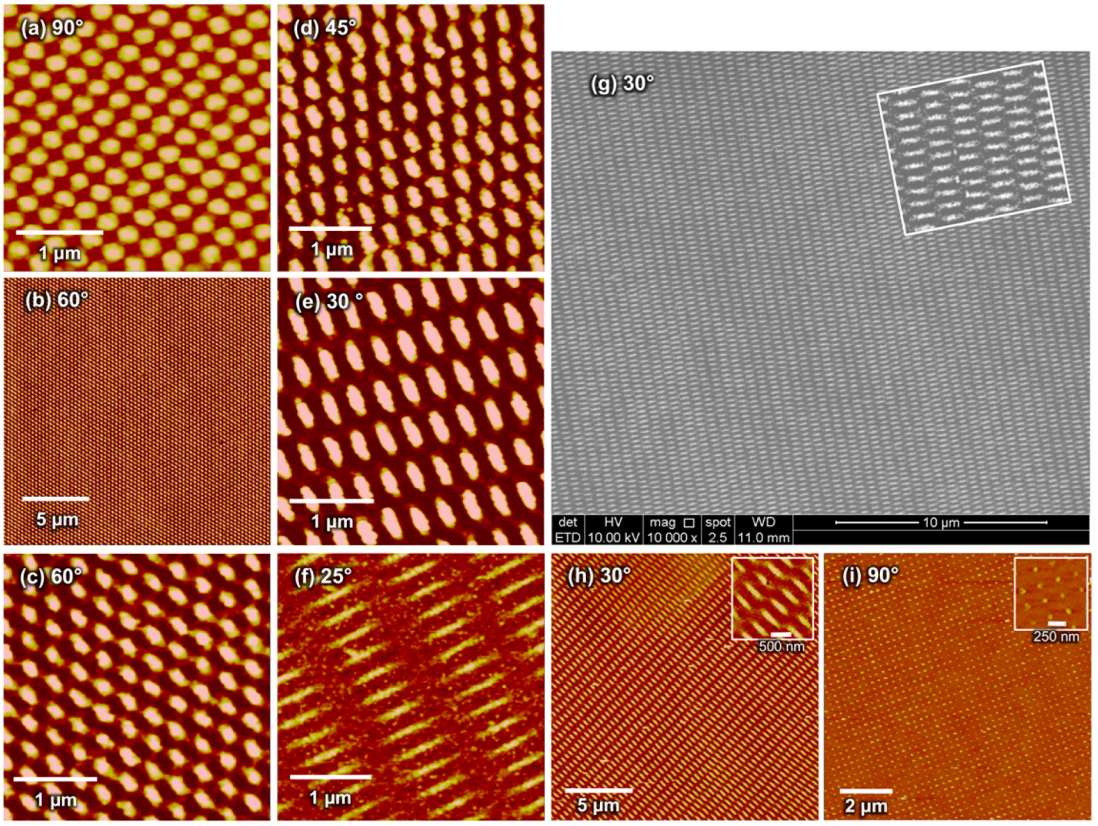

Figure 2. (a−f) AFM topographical images of as-prepared gold nanostructures fabricated using two exposures with varying angles of rotation between exposure, ϕ, of 25°, 30°, 45°, 60°, and 90°. (g) SEM image of a sample prepared using $\phi = 30°$. (h, i) AFM topographical images of as-prepared gold nanostructures fabricated using a Ti adhesion layer and two different rotations ϕ. In all images, the value of ϕ is indicated. All AFM images are adjusted to the same vertical scale for ease of comparison, with height range 0−20 nm from dark to bright contrast. Samples (a) to (g) were fabricated using a Cr adhesion layer and samples (h) and (i) with a Ti adhesion layer.

films, but without strong, unambiguous plasmon absorptions.

To analyze the sensing characteristics of the type II structures, we examined their sensitivity to the bulk refractive index (RI) by collecting the extinction spectra of nanorods surrounded by air and aqueous solutions containing 0−72% glycerol. Representative absorption spectra for gold nanorods are shown in the Supporting Information. The nanostructures were sensitive to the dielectric environment, and the resonance peaks red-shifted as the refractive index of the surrounding medium increased. Figure 4b shows the linear relationship between the refractive index and the extinction spectra peak wavelengths. The slope of the line, $m = 52.5$ nm/RIU (refractive index unit), is the refractive index sensitivity factor for that nanorod sample. There is scope for further improvement to the current system. The most effective approach would be to tune the LSPR peak by changing the size and spacing of the nanorods.

Raman spectra were acquired for films of the tetra-*tert*-butyl-substituted phthalocyanine (H_2Pc) deposited on type II nanostructures and on continuous polycrystalline gold (as a reference). First, the spectrum of solid H_2Pc was obtained as a reference and the peaks were identified and assigned (Supporting Information). The symmetry assignment of vibrations in the spectrum of H_2Pc was done on the basis of comparison with Raman spectra of unsubstituted metal-free phthalocyanine.[41]

The SERS spectra in the range 200−2000 cm^{-1} are shown in Figure 5 for H_2Pc adsorbed on both type II nanostructured surfaces and a continuous polycrystalline film. Raman bands detected on the continuous gold surface were very weak. However, a large enhancement was observed in the Raman scattering intensities for a H_2Pc film deposited on the gold nanostructures. This is attributed to strong coupling between the adsorbate and the gold plasmons. The extent of the enhancement in the Raman bands was correlated with the change in topography: in Figure 5, samples (b) and (c) consist of larger gold particles, with the denser packing in (c) yielding a larger enhancement in the Raman signal; sample (d) consists of smaller particles and yields a Raman enhancement that is still stronger.

Sample Stability and Aging. We also used AFM analysis and visible spectroscopy to investigate the stability and aging of the sample surfaces as a result of multiple reuse. The cycles included the immobilization of protein (or phthalocyanines) and spectroscopic and

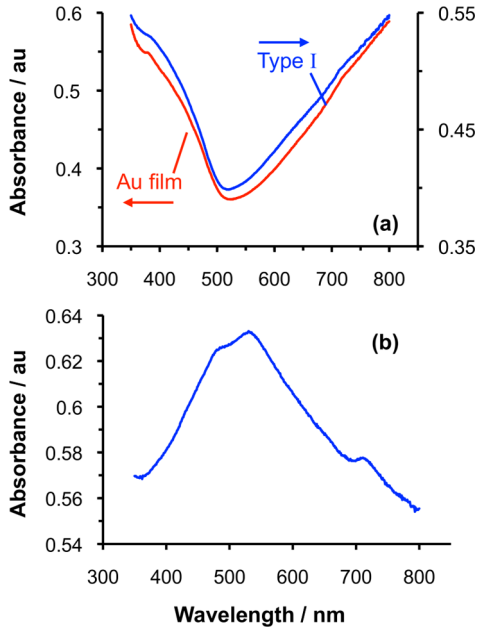

Figure 3. Absorption spectra of gold nanostructures. (a) Type I structures (blue spectrum; see text for definition), together with a spectrum acquired for a continuous polycrystalline gold film (red spectrum). (b) Spectrum acquired for a plasmonically active type II structure (see text for definition).

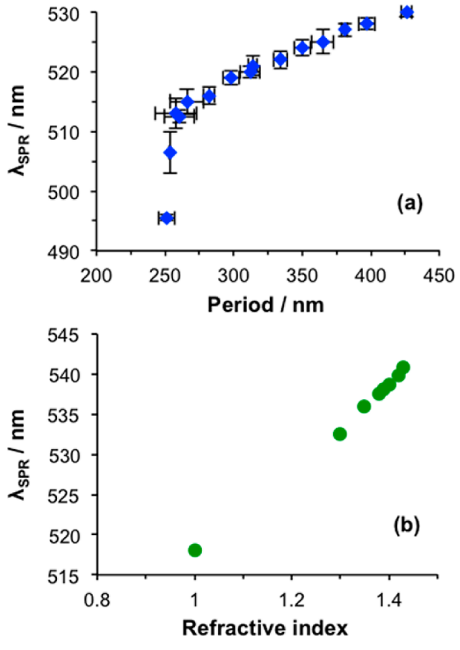

Figure 4. (a) Variation in λ_{SPR} as a function of the period (the peak-to-peak distance between rows of nanostructures). (b) Variation in λ_{SPR} as a function of the refractive index of the medium for type II structures. The error bars (not shown for the sake of clarity) are of similar size to the symbols used to mark the data points.

Raman measurements followed by washing with cold piranha solution. AFM analysis of "used" samples, subjected to multiple repeated cycles of cleaning and reuse, showed very small (less than 1%) changes in height, width, length and spacing of IL-fabricated

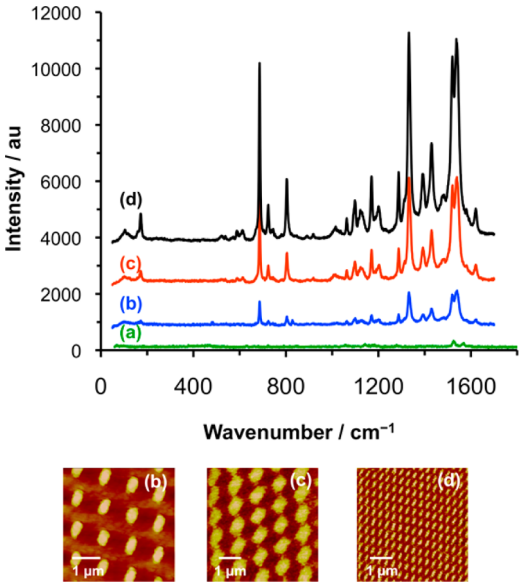

Figure 5. SERS spectra of H_2Pc on a bare gold surface and on IL-fabricated nanostructures. Spectrum (a) was acquired from a polycrystalline gold film, while spectra (b) to (d) were acquired from samples with the morphologies shown, respectively, in the AFM height images (b) to (d).

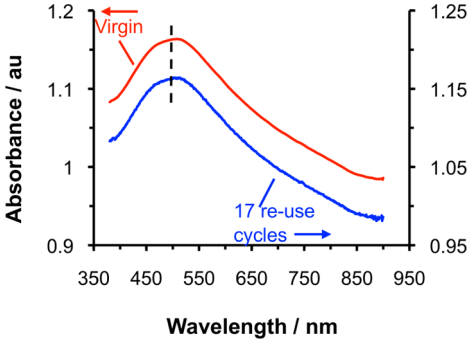

Figure 6. Absorption spectra of a type II as-prepared sample before and after 17 cycles of use, cleaning in piranha solution, and reuse.

nanostructures. Absorption spectra showed a blue shift of less than 1 nm (for example, from λ_{res} = 528 nm for virgin particles to λ_{res} = 527 nm after 20 cycles (approximately 9 months)). Some specimens have been in continuous reuse for periods as long as two years. Figure 6 shows a representative example, which has been subjected to 17 reuse cycles. The high stability of these samples is attributed to the presence of the Cr adhesion layer between the gold and the substrate, which stabilizes the gold particles under the harsh conditions during exposure to piranha solution.

Annealing. To increase their crystallinity and reduce their intrinsic granularity, type I samples were annealed in air at between 450 and 555 °C for times varying from 50 to 120 min and characterized by AFM. Annealing at temperatures above 555 °C led to complete destruction of the nanostructures. The periodic pattern was also lost when the thickness of the gold film, prior to

patterning and etching, was less than 20 nm. Figure 7a and b show representative AFM images of a sample before and after annealing at 450 °C. After annealing, the periodicity of the nanostructures was generally retained, but their dimensions changed. Annealed nanostructures were higher but smaller, laterally, than was the case before annealing. The regions between features in the as-prepared samples contain small crystallites, which disappear following annealing, and these are likely incorporated into the nanostructures during the process. Data are presented in Table 1, which show the extent of the change in dimensions that was observed for a representative selection of samples that exhibited no plasmon absorptions in their as-prepared state. AFM images of representative samples are shown in the Supporting Information. It should be noted that the errors shown for the dimensions of the structures before and after annealing may be underestimates because of the difficulty associated with determining perimeters of the nanostructures before annealing. The morphologies of the structures also changed as a result of annealing, undergoing a transition from being approximately flat-topped to approximately pyramidal in cross section.

For samples fabricated with $\phi = 30°$, the period both along and perpendicular to the rows of nanostructures is little changed by annealing, but the structures increase greatly in height (by a factor of *ca.* 6). For $\phi = 60°$, a small change in the period is observed in one direction, but again, a substantial increase in the height of the nanostructures is observed. For $\phi = 45°$, a small change in the period is observed in one direction, but the increase in height of the structures is smaller (it doubles). Finally for $\phi = 90°$, there is a small increase in period in one direction and a small decrease in the other, in addition to an increase in the height.

After annealing, all structures yielded absorbance spectra that were significantly changed and exhibited strong plasmon bands (see discussion below).

The effect of annealing was investigated by X-ray diffraction. Figure 7c and d show the reflected intensity as a function of the diffraction angle (2θ) before and after annealing (respectively) for nanostructures formed on Cr-primed substrates. A peak is observed at an angle of 38.3°, that corresponds to the (111) orientation of the cubic gold structure.[31] It can be seen that the intensity of this peak was very much increased after annealing, indicating that the annealing process caused extensive recrystallization of the gold in the nanostructures. The increased height and reduced lateral dimensions of the nanostructures are likely a consequence of this recrystallization.

Figure 7f shows X-ray data for a type II structure. The (111) peak is increased in intensity compared to the corresponding peak in Figure 7c, suggesting that the plasmonic properties of these structures may be attributable to a higher degree of crystallinity. However, the

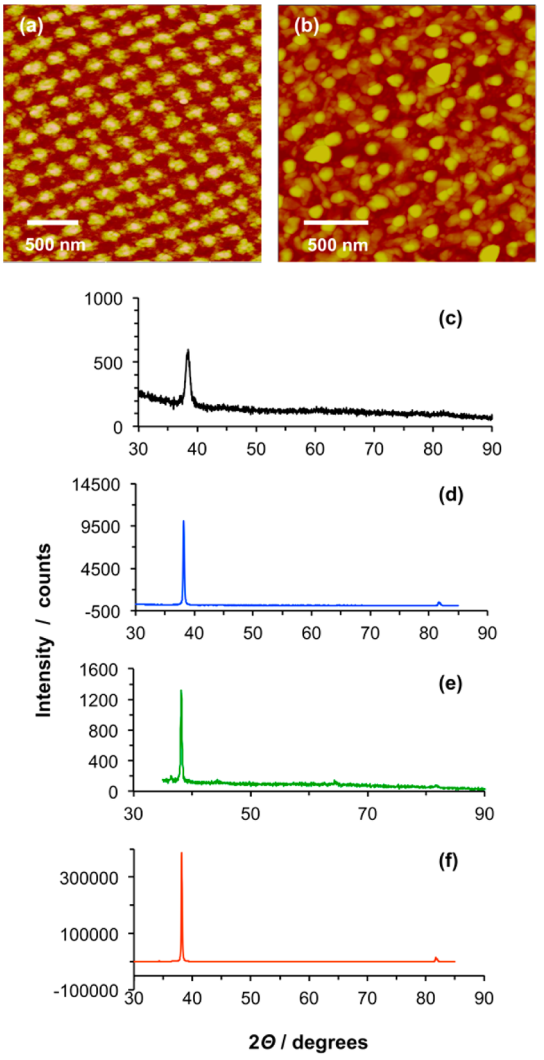

Figure 7. (a and b) AFM topographs for type I gold nanostructure arrays on Cr-primed silica before and after annealing, respectively. (c and d) Corresponding X-ray diffraction data, before and after annealing (respectively). (e) X-ray diffraction data for a type II sample, fabricated with $\phi = 30°$. (f) X-ray data for an annealed nanostructure array that was prepared on a Ti-primed substrate.

intensity of the (111) peak in Figure 7e is still very much less than that of the peak in Figure 7d.

Annealing of nanostructures formed on Ti-primed substrates also yielded a substantial increase in crystallinity (Figure 7f). However, the absorbance spectra of these samples did not exhibit plasmon peaks.

Figure 8a shows absorption spectra of a representative type I sample before and after annealing. An AFM image of this sample is shown in Figure 7a. The as-prepared sample (red spectrum) exhibits no plasmon peak and resembles the absorbance spectrum of a polycrystalline film. After annealing, however, a strong plasmon peak may be observed. The average crystal size was calculated from the X-ray data using the Scherrer equation:[42]

$$\tau = \frac{K\lambda}{\beta \cos\theta} \qquad (2)$$

TABLE 1. Effects of Annealing on the Dimensions and Optical Properties of Gold Nanostructures Formed on Cr-Primed Substrates

ϕ/deg	anneal temp/°C	anneal time/min	height/nm	length *L*/nm	width *W*/nm	*L*/*W*	period P_1/nm	period P_2/nm	λ_{SPR}/nm
30			13.7 ± 1.0	410.3 ± 41.5	120.2 ± 7.1	3.41 ± 0.4	275.9 ± 6.8	536.2 ± 5.1	absent
30	450	50	83.9 ± 10.7	238.3 ± 20.7	164.8 ± 16.3	1.45 ± 0.19	263.7 ± 23.1	510.2 ± 32.6	664
45			16.6 ± 1.8	228.7 ± 12.8	142.6 ± 6.9	1.60 ± 0.12	263.3 ± 5.2	374.0 ± 9.9	absent
45	490	120	31.9 ± 1.0	153.4 ± 17.9	112.2 ± 11.8	1.37 ± 0.21	261.3 ± 10.9	271.0 ± 10.6	565
60			18.3 ± 1.8	776.0 ± 78.0	366 ± 37	2.12 ± 0.3	648.7 ± 6.1	787.0 ± 24.1	absent
60	470	120	143 ± 16.2	513.4 ± 30.3	332.3 ± 3.1	1.54 ± 0.1	622.3 ± 55.0	683.0 ± 52.3	594
90			12.9 ± 1.1	183.2 ± 11.9	127.9 ± 12.7	1.43 ± 0.17	208.9 ± 5.2	242.1 ± 9.3	absent
90	470	120	43.3 ± 4.5	122.2 ± 12.2	89.5 ± 7.3	1.36 ± 0.17	228.5 ± 13.9	149.7 ± 10.8	569

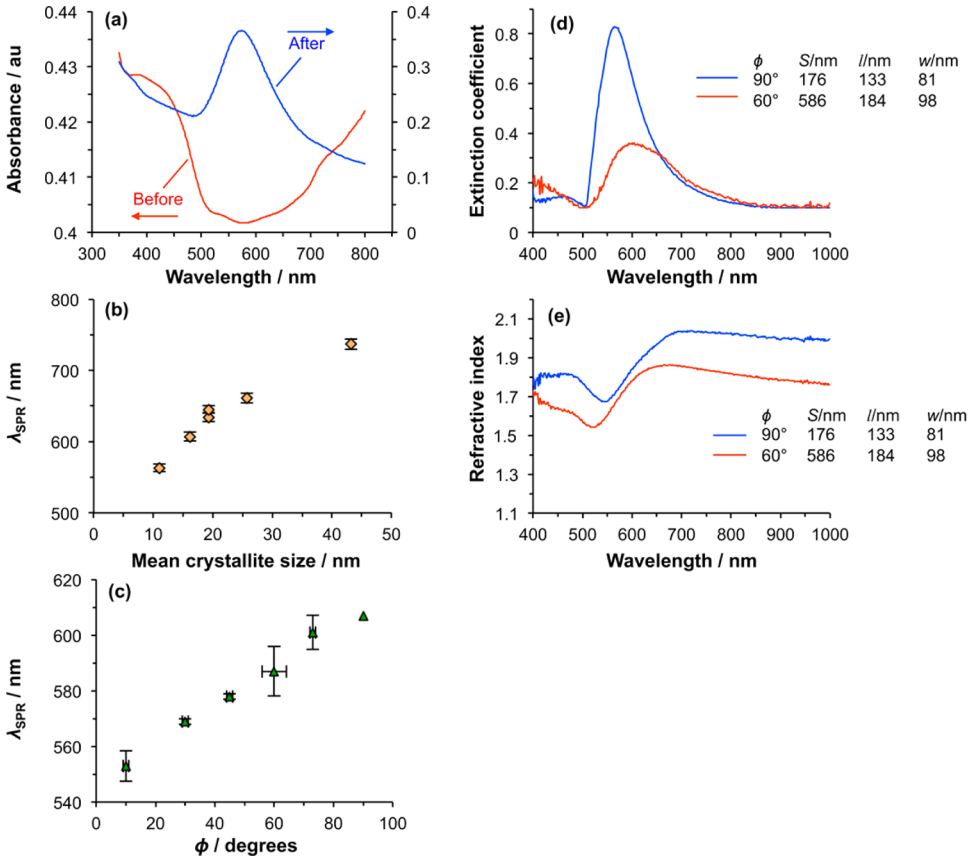

Figure 8. (a) Absorption spectrum of a type I sample, fabricated with $\phi = 90°$, before (red) and after (blue) annealing, acquired using a spectrophotometer. (b) Variation in the position of the plasmon peak, λ_{SPR}, as a function of crystallite size for a large number of samples consisting of annealed nanostructures. (c) Variation in the position of the plasmon peak, λ_{SPR}, as a function of the angle of rotation ϕ between exposures for annealed samples. (d) Variation in the extinction coefficient with wavelength, determined by fitting of ellipsometry data, for two representative samples fabricated with $\phi = 90°$ and 60° after annealing. (e) Variation in the refractive index with wavelength, determined by fitting of ellipsometry data, for two representative samples fabricated with $\phi = 90°$ and 60° after annealing.

where *K* is an instrumental constant, λ is the X-ray wavelength, β is the line broadening at half the maximum intensity in radians, and θ is the Bragg angle. The sizes of the gold crystals at the diffraction angles of 38.3° and 81.75° (one with the strongest reflected intensity) varied from *ca.* 19 to 66 nm depending on the sample morphology. The position of the plasmon peak in the absorbance spectrum, λ_{SPR}, was found to change with the crystallite size (Figure 8b), becoming increasingly red-shifted as the crystallite size increased. In these specimens, the mean crystallite size was smaller than the particle size; the increase in crystallite size likely means a larger crystalline fraction, and this probably accounts for the change in optical properties.

The angle of rotation between exposures, ϕ, was found to be strongly correlated with the position of the plasmon peak in the absorbance spectrum. Figure 8c shows mean data for a large number of samples.

The relationship between λ_{SPR} and ϕ was found to be linear, meaning that samples could be prepared to yield a specific λ_{SPR} value simply by setting ϕ to an appropriate value during the lithographic process. For a given, fixed angle 2θ between the two interfering beams in the interferometer, control of ϕ enables selection of λ_{SPR}.

Annealed samples were characterized by spectroscopic ellipsometry. A fitting procedure was applied to the ellipsometric spectra to adjust the free parameters of the dielectric functions and thickness of the nanostructured layer. The nanostructured gold films were modeled assuming Au to be semitransparent. The optical constants of the gold as well as thickness of the gold layer were modeled using the generalized oscillation layer summed with Drude oscillators.[42,43] The Cr layer and the BK7 glass substrate were also included in the model. The following discussion is focused on samples fabricated with values of ϕ of 90° and 60°.

Dependences of the refractive index n and extinction coefficient k on light wavelength λ, derived from the ellipsometric data, are shown in Figure 8d. Both optical constants n and k undergo changes: as seen in the graph, relatively sharp peaks in the value of the extinction coefficient are detected at approximately 560−600 nm, shifting toward longer wavelength with increasing diameter of the nanostructures. The range of k decreases from *ca.* 1.5−5.5 to 0.1−0.85 for as-prepared and annealed samples, respectively.

The refractive indices of all annealed samples had local minima in the range 520 to 540 nm, also shifting toward longer wavelength as the sizes of the nanostructures increased. For annealed samples all changes in the refractive index were observed over a relatively small range, from *ca.* 1.2 to 2.1, over the measured spectral range (400−1000 nm). For the as-prepared samples, the refractive index varied over a larger range, from *ca.* 0.2 to 2.0.

RI Sensitivity of Annealed Gold Nanostructures. The LSPR response of the annealed nanostructures to changes in the bulk refractive index was investigated for a series of samples fabricated with $\phi = 30°$. In order to obtain the refractive index sensitivity m ($m = \Delta\lambda_{SPR}/\Delta n$), UV−visible absorption spectra were measured in media with different refractive indices: ethanol and 1:1, 1:2, 1:25, and 1:3 water−glycerol mixtures. The resulting variation in λ_{SPR} as a function of the refractive index n of the medium is shown in Figure 9. The LSPR wavelength increases monotonically with n. The RI sensitivity of the annealed samples was found to be 145 nm/RIU. This value is significantly larger than that of the as-prepared samples (m = 52.5 nm/RIU), because of the smaller sizes of the nanostructures and the larger spacing between them.

The refractive index sensitivity is shown as a function of the interparticle spacing in Figure 9b. Our

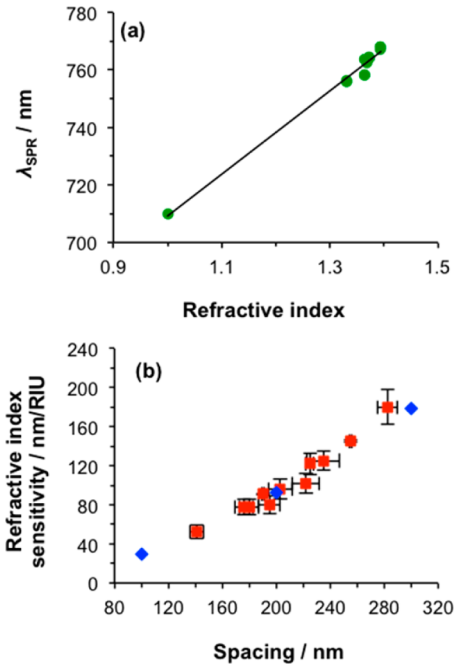

Figure 9. (a) Variation in the position of the plasmon peak with the refractive index of the medium. The error bars are of similar size to the symbols used to mark the points. (b) Variation in the refractive index sensitivity with the spacing between nanostructures fabricated with ϕ = 30°. Red squares: this study. Blue diamonds: data from Vazquez-Mena *et al.* for gold nanostructures formed using stencil lithography.[40]

experimental data (red squares) correlated well with data reported by Vazquez-Mena *et al.* (blue diamonds) for samples prepared by evaporation of gold through a stencil mask.[40] The RI sensitivity increases with the interparticle separation. For instance, an as-prepared sample with a spacing of *ca.* 141 nm has an RI sensitivity of 52.5 nm/RIU, and an annealed sample with a spacing of *ca.* 255 nm has an RI sensitivity of 145 nm/RIU. The RI sensitivities obtained by Vazquez-Mena *et al.* were m = 179 nm/RIU for nanodots with spacing S = 300 nm, m = 93 nm/RIU for S = 200 nm, and m = 30 nm/RIU for S = 100 nm.

Sensing Properties of Annealed Samples. IL enables the rapid production of samples with varying structures, enabling their suitability for sensing applications to be evaluated systematically and conveniently. To demonstrate the value of this capability, a library of samples was prepared using a constant angle 2θ between the sample and the mirror in the interferometer, but a varying angle ϕ (as used to generate the data shown in Figure 8c). These were screened for their suitability in detecting histidine-tagged green fluorescent protein (His-GFP) and bacteriochlorophyll *a* (BChl *a*). The BChl *a* was simply physisorbed onto the gold nanostructures. His-GFP was bound *via* site-specific attachment: gold nanostructures were functionalized with aminoundecanethiol, which was derivatized with glutaraldehyde and then aminobutyl nitrilotriacetic acid (ABNTA).

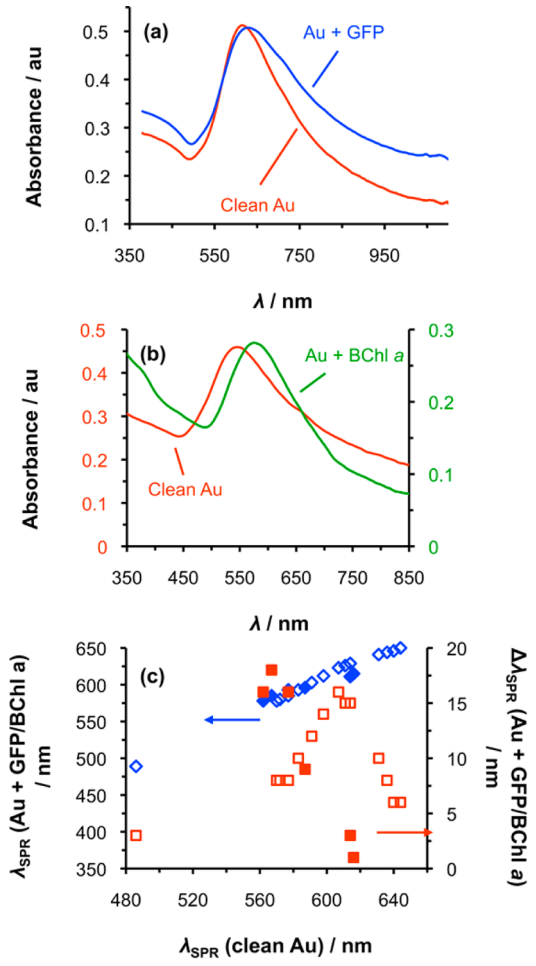

Figure 10. (a) Absorbance spectra of a gold nanostructure array before and after adsorption of histidine-tagged green fluorescent protein (His-GFP), showing a red shift of 15 nm in the position of the plasmon peak after adsorption of the protein. (b) Absorbance spectra of a gold nanostructure array before and after adsorption of bacteriochlorophyll *a*. (c) Variation in λ_{SPR} (blue diamonds, left-hand vertical axis) and the shift in the position of the plasmon peak (red squares, right-hand vertical axis) after adsorption of His-GFP (open symbols) and bacteriochlorophyll *a* (filled symbols) onto a wide range of samples consisting of nanostructures with varying periods and dimensions. The error bars are of similar size to the symbols used to mark the points.

After complexation with Ni^{2+}, NTA coordinates strongly to a His_6 tag, which may conveniently be introduced into the peptide sequences of many proteins. The protocol provides a simple and effective means for site-specific immobilization of proteins.

Figure 10a shows illustrative spectra of a clean gold nanostructure array and the same structure following deposition of GFP. It can be seen that the plasmon peak is shifted to a longer wavelength after adsorption of the protein. Figure 10b shows spectra acquired before and after adsorption of BChl *a*. Again, it can be seen that the plasmon peak is shifted to longer wavelength by adsorption of the biomolecule. Figure 10c shows data for the full series of samples. The diamonds (left-hand vertical axis) show the variation in the value of λ_{SPR} after protein adsorption as a function of the value of λ_{SPR} for the clean gold nanostructures. It can be seen that the relationship is nonlinear: the size of the increase in λ_{SPR} after adsorption of GFP varies across the series. The squares (right-hand axis) show the variation in the shift in the position of the plasmon peak, $\Delta\lambda_{SPR}$, as a function of λ_{SPR} for the clean nanostructures. The variation in $\Delta\lambda_{SPR}$ is quite sharply peaked for His-GFP, at 15 nm for a sample that when clean yields a plasmon peak at *ca.* 610 nm. For BChl *a*, however, the plot of $\Delta\lambda_{SPR}$ as a function of λ_{SPR} peaks at *ca.* 570 nm. The same nanostructured sample yields a much smaller shift in the plasmon band for His-GFP.

The capacity to search a library of structures quickly and easily for ones that yield optimal responses (in this case, the largest shift in the position of the plasmon peak) in such a combinatorial fashion is a significant benefit of our approach and reflects the fact that IL enables the fast fabrication of structures with varying but controllable dimensions. Samples may be cleaned by immersion in piranha solution and reused, allowing repeated measurements on the same set to explore how the optical response varies with the structure of the biological molecule or other dye.

CONCLUSIONS

Interferometric lithography of self-assembled monolayers of alkylthiolates on gold, combined with wet etching by mercaptoethylamine and ammonia in ethanol, provides a rapid, simple method for the fabrication of arrays of gold nanostructures over macroscopic areas. Apart from the laser, only very simple optical components are required. The period and dimensions of the resulting nanoparticle arrays are readily controllable and, moreover, may be selected by varying the exposure time, sample−mirror angle, angle of rotation between exposures, and etch time. The use of Cr as an adhesion primer prior to Au film formation yields nanostructure arrays that are robust enough to be cleaned in cold piranha solution and reused repeatedly. Annealing yields nanostructures with a high degree of crystallinity and very good optical properties, including strong plasmon bands. Significant enhancements are observed in Raman scattering, and substantial shifts are observed in the position of the plasmon band. We think it likely that the plasmonic properties of the structures, whether annealed or not, are controlled by a combination of degree of crystallinity, crystallite size, nanostructure dimensions, and period. The variation in ϕ during the fabrication process likely has a strong effect on the latter two parameters, and the annealing process influences the first two, although to some extent, ϕ may also influence the crystallinity of the structures in a way that is not, at present, clear. Because of the capacity of our methodology to fabricate nanostructures in a combinatorial fashion, it is possible to survey large collections of

structures to identify those that are best suited for a particular analyte. As plasmonics becomes a mature field and has increasing impact on analytical chemistry, this capacity, combined with the availability of durable samples capable of multiple reuse, is expected to be very valuable.

EXPERIMENTAL SECTION

Preparation of SAMs. Glass microscope slides (Menzel-Gläser) and glass vials were cleaned by immersion for 1 h in piranha solution, a mixture of 30% hydrogen peroxide and concentrated (95%) sulfuric acid in the ratio 3:7. Cleaned glass microscope slides were coated with a *ca.* 2−5 nm thick chromium film followed by a nominal thickness of 20 nm gold layer (the nominal thickness is the reading of the evaporator QCM thickness monitor, *i.e.*, the film mass thickness). Chromium, titanium, and gold were both deposited using an Edwards Auto 306 bell jar vacuum coater system under a pressure of 8×10^{-7} mbar. Evaporation rates of *ca.* 0.1 nm s^{-1} for Cr and Ti and up to 0.4 nm s^{-1} for Au were used.

Coated glass slides were immersed overnight in 1 mmol solutions of octadecanethiol (Sigma-Aldrich) in degassed ethanol (HPLC purity, Sigma-Aldrich) to form closely packed self-assembled monolayers. Glass slides can be kept in ODT up to 6 month. Before UV exposure they were sonicated for 1−2 min, rinsed with ethanol, and blown dry with nitrogen.

Interferometric Lithography. UV light at 244 nm from a Coherent Innova 300C FreD frequency-doubled argon ion laser was used as a light source for photolithography. The laser beam was focused by a lens through a spatial filter with an aperture of 5 μm to obtain a coherent beam. The edge of the coherent beam was cut by using a mask with a suitable aperture.

Photopatterned ODT monolayers on gold films were etched by immersion in a 0.2 mol dm^{-3} solution of 2-mercaptoethylamine hydrochloride in 8% v/v of 35% of ammonia (obtained from Fisher Scientific) in ethanol (Sigma-Aldrich Co.). After etching, the samples were rinsed in ethanol and dried with nitrogen gas.

Annealing of gold nanostructures was carried out in air at 450−555 °C for various times (50−120 min) using a muffle furnace (Carbolite). The heating rate was *ca.* 7 °C min^{-1}, and the annealed samples were left to cool in air to room temperature.

Samples were cleaned for reuse by immersion in cold piranha solution (a mixture of 30% hydrogen peroxide and concentrated sulfuric acid in the ratio 3:7 that had been allowed to cool to room temperature) for 5−7 min. *Caution: piranha solution is a very strong oxidizing agent and may react violently with organic materials*. After cleaning, they were rinsed in deionized water and blown dry with nitrogen.

Characterization. Atomic force microscopy (AFM) images were acquired in air using a Digital Instruments Nanoscope Multimode IIIa atomic force microscope operated in tapping and contact modes. The probes used for contact mode were the NP-10 series of silicon nitride (Bruker) with spring constant k = 0.06 or 0.12 N m^{-1}. For tapping mode, RTESP probes (nominal tip radius 8 nm) and TESP-SS series ultrasharp silicon probes (Bruker) were used, with a resonance frequency of 320−350 kHz and an average tip radius of 2 nm.

Scanning electron microscopy (SEM) images were obtained using a FEI Nova Nano SEM-200 scanning electron microscope. Low-energy (3−10 kV) secondary electron signal suppression was performed to reduce the charging effects.

Raman scattering spectra of tetra-*tert*-butylsubstituted phthalocyanine H_2Pc (2,9,16,23-tetra-*tert*-butyl-29*H*,31*H*-phthalocyanine, obtained from Sigma-Aldrich) on gold nanostructures were measured by a confocal Raman spectrometer (Lab RAM HR 800, Horiba Scientific) fitted with CCD spectrometric detectors and a microscope attachment. The 532 nm solid-state diode laser line (0.5 mW) was used for spectral excitation. The laser beam focused onto the sample by a microscope objective with 100-fold magnification (numerical aperture (NA) = 0.9); the diameter of an incident laser beam was approximately 1 μm. The spectral resolution was about 2 cm^{-1}. Raman scattering frequency for each Raman line remained constant from sample to sample, deviating less than 2 cm^{-1}. Samples of Au nanostructures that were fabricated using the IL technique were cleaned in cold piranha solution for 7 min, rinsed with deionized water, blown dry with nitrogen, and immersed in 0.1 mg mL^{-1} phthalocyanine in chloroform (Sigma-Aldrich Co.) solution for 1 h to form a self-assembled monolayer. Finally, samples were rinsed with chloroform in order to remove excess phthalocyanine and then gently dried with nitrogen.

Optical properties of the fabricated structures were determined from spectrophotometry and variable-angle spectroscopic ellipsometry measurements. UV−visible absorption spectra at normal incidence were recorded using a Hitachi U-3010 double-beam spectrophotometer and a Cary 50 spectrophotometer. The wavelength scan range was 350−800 nm (unless otherwise stated). The samples were placed in a special holder, enabling absorption measurements of the same spot on the sample during all experimental stages. Data processing included smoothing and identification of the absorbance maximum using a derivative routine.

The variable-angle spectroscopic ellipsometer M-2000-V (J. A. Woollam Co. Inc.) was used to record the change in light beam polarization under its reflection from as-prepared and annealed gold nanostructures in the spectral range 370−1000 nm. The angle of incidence was set at 45° and 70°. Ellipsometric data were acquired and analyzed using the CompleteEASE software program. The same two points were measured on each sample before and after annealing.

Structural characterization of annealed samples was performed by X-ray diffraction (XRD) analysis using a Philips X'pert-MPD diffraction system with an ultrafast semiconductor detector, PIXcel. The X-ray source was a long-fine-focus, ceramic X-ray tube with Cu anode. The operating power was 40 kV, 50 mA (2.0 kW). The irradiated area of the sample was 1.5×1.5 mm^2. Acquired data enabled the determination of particle size and crystallographic orientation of the IL-fabricated nanostructures.

In order to investigate the biosensing capabilities of as-prepared and annealed samples fabricated by IL, the LSPR response of nanostructures to changes in the refractive index of the surrounding media was measured. In order to obtain the refractive index sensitivity m ($m = \Delta\lambda_{res}/\Delta n$), the UV−visible absorption spectra were measured in media with different refractive indices. Water−glycerol mixtures of varying volume ratios and ethanol were used to change the refractive index of the surrounding medium of gold nanostructures. The volume percentage of glycerol in the liquid mixture was varied from 0% to 72%. The refractive index of the liquid mixture was calculated according to the Lorentz−Lorenz equation:[44]

$$\frac{n_{12}^2 - 1}{n_{12}^2 + 2} = \varphi_1 \frac{n_1^2 - 1}{n_1^2 + 2} + \varphi_2 \frac{n_2^2 - 1}{n_2^2 + 2} \quad (3)$$

where n_{12} is the refractive index of the liquid mixture, n_1 and n_2 are the indices of water (1.3334) and glycerol (1.4746), respectively, and φ_1 and φ_2 are the volume fractions of the two components.

His_6-GFP was produced by heterologous expression in *E. coli* (BL21); cells were grown to an OD_{680} of 0.6 at 37 °C, then induced using IPTG (0.4 mM) for 12 h at 25 °C. Pelleted cells (19000*g*/20 min) were lysed by sonication, and the resulting lysate was clarified by a further spin (33000*g*/30 min). His-tagged fluorescent protein was purified to homogeneity from clarified lysate using a Chelating Sepharose Fast Flow Ni-NTA gravity flow column (GE Healthcare) as detailed in the manufacturer's instructions. Protein purity was assessed by gel electrophoresis (SDS-PAGE). Gold nanostructure arrays were functionalized with aminoundecanethiol by immersion in a 1 mmol solution in ethanol, washed with ethanol, dried, and derivatized

with glutaraldehyde (12.5% in water) and then in a 20 mM aqueous solution of AB-NTA for 2 h. The samples were rinsed with deionized water, blown dry with nitrogen, and immersed in a 10 mM aqueous solution of nickel sulfate for 5 min to ensure complexation of NTA by Ni^{2+}. The samples were washed thoroughly with deionized water and blown dry with nitrogen to remove excess Ni^{2+}. The samples were then immersed in His-GFP solution diluted with 20 mM Tris buffer in the ratio of 1:20. The surfaces were left immersed in the protein solution for 24 h in a humid chamber. The samples were then gently washed by repeatedly dipping in deionized water and dried under nitrogen.

Conflict of Interest: The authors declare no competing financial interest.

Supporting Information Available: Further details on the characterization of gold nanostructures by AFM and optical methods, together with a detailed assignment of the peaks in the H_2Pc Raman spectrum. This material is available free of charge *via* the Internet at http://pubs.acs.org.

Acknowledgment. The authors are grateful to EPSRC (Grants EP/H050132/1 and EP/I012060/1) for financial support. C.N.H. and G.J.L. also acknowledge funding from the Biotechnology and Biological Sciences Research Council (U.K.). T.B. acknowledges funding from the Ministry of Education and Science of the Russian Federation (Project No. 14.BBB.21.0206).

REFERENCES AND NOTES

1. Maier, S. A.; Brongersma, M. L.; Kik, P. G.; Meltzer, S.; Requicha, A. A. G.; Atwater, H. A. A Route to Nanoscale Optical Devices. *Adv. Mater.* **2001**, *13*, 1501–1505.
2. Barnes, W. L.; Dereux, A.; Ebbesen, T. W. Surface Plasmon Subwavelength Optics. *Nature* **2003**, *424*, 824–830.
3. Gray, S. K. Theory and Modeling of Plasmonic Structures. *J. Phys. Chem. C* **2012**, *117*, 1983–1994.
4. Ergin, T.; Stenger, N.; Brenner, P.; Pendry, J. B.; Wegener, M. Three-Dimensional Invisibility Cloak at Optical Wavelengths. *Science* **2010**, *328*, 337–339.
5. Fang, N.; Lee, H.; Sun, C.; Zhang, X. Sub−Diffraction-Limited Optical Imaging with a Silver Superlens. *Science* **2005**, *308*, 534–537.
6. Hibbins, A. P.; Evans, B. R.; Sambles, J. R. Experimental Verification of Designer Surface Plasmons. *Science* **2005**, *308*, 670–672.
7. Ebbesen, T. W.; Lezec, H. J.; Ghaemi, H. F.; Thio, T.; Wolff, P. A. Extraordinary Optical Transmission through Sub-Wavelength Hole Arrays. *Nature* **1998**, *391*, 667–669.
8. Anker, J. N.; Hall, W. P.; Lyandres, O.; Shah, N. C.; Zhao, J.; Van Duyne, R. P. Biosensing with Plasmonic Nanosensors. *Nat. Mater.* **2008**, *7*, 442–453.
9. Prodan, E.; Radloff, C.; Halas, N. J.; Nordlander, P. A Hybridization Model for the Plasmon Response of Complex Nanostructures. *Science* **2003**, *302*, 419–422.
10. Link, S.; Mohamed, M. B.; El-Sayed, M. A. Simulation of the Optical Absorption Spectra of Gold Nanorods as a Function of their Aspect Ratio and the Effect of the Medium Dielectric Constant. *J. Phys. Chem. B* **1999**, *103*, 3073–3077.
11. Rosi, N. L.; Mirkin, C. A. Nanostructures in Biodiagnostics. *Chem. Rev.* **2005**, *105*, 1547–1562.
12. Jageler-Hoheisel, T.; Cordeiro, J.; Lecarme, O.; Cuche, A. l.; Girard, C.; Dujardin, E.; Peyrade, D.; Arbouet, A. Plasmonic Shaping in Gold Nanoparticle Three-Dimensional Assemblies. *J. Phys. Chem. C* **2013**, *117*, 23126–23132.
13. Elghanian, R.; Storhoff, J. J.; Mucic, R. C.; Letsinger, R. L.; Mirkin, C. A. Selective Colorimetric Detection of Polynucleotides Based on the Distance-Dependent Optical Properties of Gold Nanoparticles. *Science* **1997**, *277*, 1078–1081.
14. Valsecchi, C.; Brolo, A. G. Periodic Metallic Nanostructures as Plasmonic Chemical Sensors. *Langmuir* **2013**, *29*, 5638–5649.
15. Lee, S.-W.; Lee, K.-S.; Ahn, J.; Lee, J.-J.; Kim, M.-G.; Shin, Y.-B. Highly Sensitive Biosensing Using Arrays of Plasmonic Au Nanodisks Realized by Nanoimprint Lithography. *ACS Nano* **2011**, *5*, 897–904.
16. Nie, S.; Emory, S. R. Probing Single Molecules and Single Nanoparticles by Surface-Enhanced Raman Scattering. *Science* **1997**, *275*, 1102.
17. Chen, S.-Y.; Mock, J. J.; Hill, R. T.; Chilkoti, A.; Smith, D. R.; Lazarides, A. A. Gold Nanoparticles on Polarizable Surfaces as Raman Scattering Antennas. *ACS Nano* **2010**, *4*, 6535–6546.
18. Chen, S.; Svedendahl, M.; Antosiewicz, T. J.; Kall, M. Plasmon-Enhanced Enzyme-Linked Immunosorbent Assay on Large Arrays of Individual Particles Made by Electron Beam Lithography. *ACS Nano* **2013**, *7*, 8824–8832.
19. Langguth, L.; Punj, D.; Wenger, J. R. M.; Koenderink, A. F. Plasmonic Band Structure Controls Single-Molecule Fluorescence. *ACS Nano* **2013**, *7*, 8840–8848.
20. Bujak, Å.; Czechowski, N.; Piatkowski, D.; Litvin, R.; Mackowski, S.; Brotosudarmo, T. H. P.; Cogdell, R. J.; Pichler, S.; Heiss, W. Fluorescence Enhancement of Light-Harvesting Complex 2 from Purple Bacteria Coupled to Spherical Gold Nanoparticles. *Appl. Phys. Lett.* **2011**, *99*, 173701.
21. Cao, Y. C.; Jin, R.; Mirkin, C. A. Nanoparticles with Raman Spectroscopic Fingerprints for DNA and RNA Detection. *Science* **2002**, *297*, 1536–1540.
22. Graham, D.; Thompson, D. G.; Smith, W. E.; Faulds, K. Control of Enhanced Raman Scattering Using a DNA-Based Assembly Process of Dye-Coded Nanoparticles. *Nat. Nanotechnol.* **2008**, *3*, 548–551.
23. Talley, C. E.; Jackson, J. B.; Oubre, C.; Grady, N. K.; Hollars, C. W.; Lane, S. M.; Huser, T. R.; Nordlander, P.; Halas, N. J. Surface-Enhanced Raman Scattering from Individual Au Nanoparticles and Nanoparticle Dimer Substrates. *Nano Lett.* **2005**, *5*, 1569–1574.
24. Qian, X.; Zhou, X.; Nie, S. Surface-Enhanced Raman Nanoparticle Beacons Based on Bioconjugated Gold Nanocrystals and Long Range Plasmonic Coupling. *J. Am. Chem. Soc.* **2008**, *130*, 14934–14935.
25. Grabar, K. C.; Freeman, R. G.; Hommer, M. B.; Natan, M. J. Preparation and Characterization of Au Colloid Monolayers. *Anal. Chem.* **1995**, *67*, 735–743.
26. Brust, M.; Fink, J.; Bethell, D.; Schiffrin, D. J.; Kiely, C. Synthesis and Reactions of Functionalised Gold Nanoparticles. *Chem. Commun.* **1995**, 1655–1656.
27. Kuznetsov, A. I.; Evlyukhin, A. B.; Goncalves, M. R.; Reinhardt, C.; Koroleva, A.; Arnedillo, M. L.; Kiyan, R.; Marti, O.; Chichkov, B. N. Laser Fabrication of Large-Scale Nanoparticle Arrays for Sensing Applications. *ACS Nano* **2011**, *5*, 4843–4849.
28. Wong, T. I.; Han, S.; Wu, L.; Wang, Y.; Deng, J.; Tan, C. Y.; Bai, P.; Loke, Y. C.; Yang, X. D.; Tse, M. S.; *et al.* High Throughput and High Yield Nanofabrication of Precisely Designed Gold Nanohole Arrays for Fluorescence Enhanced Detection of Biomarkers. *Lab Chip* **2013**, *13*, 2405–2413.
29. Nagpal, P.; Lindquist, N. C.; Oh, S.-H.; Norris, D. J. Ultrasmooth Patterned Metals for Plasmonics and Metamaterials. *Science* **2009**, *325*, 594–597.
30. Michel, R.; Lussi, J. W.; Csucs, G.; Reviakine, I.; Danuser, G.; Ketterer, B.; Hubbell, J. A.; Textor, M.; Spencer, N. D. Selective Molecular Assembly Patterning: A New Approach to Micro- and Nanochemical Patterning of Surfaces for Biological Applications. *Langmuir* **2002**, *18*, 3281–3287.
31. Denis, F. A.; Harnap, P.; Sutherland, D. S.; Dufrene, Y. F. Nanoscale Chemical Patterns Fabricated by Using Colloidal Lithography and Self-Assembled Monolayers. *Langmuir* **2004**, *20*, 9335–9339.
32. Menezes, J. W.; Ferreira, J.; Santos, M. J. L.; Cescato, L.; Brolo, A. G. Large-Area Fabrication of Periodic Arrays of Nanoholes in Metal Films and their Application in Biosensing and Plasmonic-Enhanced Photovoltaics. *Adv. Funct. Mater.* **2010**, *20*, 3918–3924.
33. Huntington, M. D.; Odom, T. W. A Portable, Benchtop Photolithography System Based on a Solid-State Light Source. *Small* **2011**, *7*, 3105–3105.
34. Brueck, S. R. J. Optical and Interferometric Lithography - Nanotechnology Enablers. *Proc. IEEE* **2005**, *93*, 1704–1721.

35. Lu, C.; Lipson, R. H. Interference Lithography: a Powerful Tool for Fabricating Periodic Structures. *Laser Photon. Rev.* **2009**, 1–13.
36. Henzie, J.; Lee, M. H.; Odom, T. W. Multiscale Patterning of Plasmonic Metamaterials. *Nat. Nanotechnol.* **2007**, *2*, 549–554.
37. Love, J. C.; Estroff, L. A.; Kriebel, J. K.; Nuzzo, R. G.; Whitesides, G. M. Self-Assembled Monolayers of Thiolates on Metals as a Form of Nanotechnology. *Chem. Rev.* **2005**, *105*, 1103–1170.
38. Adams, J.; Tizazu, G.; Janusz, S.; Brueck, S. R. J.; Lopez, G. P.; Leggett, G. J. Large-Area Nanopatterning of Self-Assembled Monolayers of Alkanethiolates by Interferometric Lithography. *Langmuir* **2010**, *26*, 13600–13606.
39. Ducker, R. E.; Leggett, G. J. A Mild Etch for the Fabrication of Three-Dimensional Nanostructures in Gold. *J. Am. Chem. Soc.* **2006**, *128*, 392–393.
40. Vazquez-Mena, O.; Sannomiya, T.; Villanueva, L. G.; Voros, J.; Brugger, J. Metallic Nanodot Arrays by Stencil Lithography for Plasmonic Biosensing Applications. *ACS Nano* **2010**, *5*, 844–853.
41. Aroca, R.; DiLella, D. P.; Loutfy, R. O. Raman Spectra of Solid Films - I: Metal-Free Phthalocyanine. *J. Phys. Chem. Solids* **1982**, *43*, 707–711.
42. Khabari, A.; Urban, F. K.; Griffiths, P.; Petrov, I.; Kim, Y.-W.; Bungay, C. Nanoparticle Beam Formation and Investigation of Gold Nanostructured Films. *J. Vac. Sci. Technol. B* **2003**, *21*, 2313–2318.
43. Loncaric, M.; Sancho-Parramon, J.; Hrvoje, Z. Optical Properties of Gold Island Films — a Spectroscopic Ellipsometry Study. *Thin Solid Films* **2011**, *519*, 2946–2950.
44. Chen, H.; Kou, X.; Yang, Z.; Ni, W.; Wang, J. Shape- and Size-Dependent Refractive Index Sensitivity of Gold Nanoparticles. *Langmuir* **2008**, *24*, 5233–5237.